

Predicting Solar Flares Using a Long Short-Term Memory Network

HAO LIU,^{1,2} CHANG LIU,^{1,3,4} JASON T. L. WANG,^{1,2} AND HAIMIN WANG^{1,3,4}

¹*Institute for Space Weather Sciences, New Jersey Institute of Technology, University Heights, Newark, NJ 07102-1982, USA*
hl422@njit.edu, chang.liu@njit.edu, wangj@njit.edu, haimin.wang@njit.edu

²*Department of Computer Science, New Jersey Institute of Technology, University Heights, Newark, NJ 07102-1982, USA*

³*Big Bear Solar Observatory, New Jersey Institute of Technology, 40386 North Shore Lane, Big Bear City, CA 92314-9672, USA*

⁴*Center for Solar-Terrestrial Research, New Jersey Institute of Technology, University Heights, Newark, NJ 07102-1982, USA*

ABSTRACT

We present a long short-term memory (LSTM) network for predicting whether an active region (AR) would produce a Υ -class flare within the next 24 hours. We consider three Υ classes, namely $\geq M5.0$ class, $\geq M$ class, and $\geq C$ class, and build three LSTM models separately, each corresponding to a Υ class. Each LSTM model is used to make predictions of its corresponding Υ -class flares. The essence of our approach is to model data samples in an AR as time series and use LSTMs to capture temporal information of the data samples. Each data sample has 40 features including 25 magnetic parameters obtained from the Space-weather HMI Active Region Patches (SHARP) and related data products as well as 15 flare history parameters. We survey the flare events that occurred from 2010 May to 2018 May, using the *GOES* X-ray flare catalogs provided by the National Centers for Environmental Information (NCEI), and select flares with identified ARs in the NCEI flare catalogs. These flare events are used to build the labels (positive vs. negative) of the data samples. Experimental results show that (i) using only 14-22 most important features including both flare history and magnetic parameters can achieve better performance than using all the 40 features together; (ii) our LSTM network outperforms related machine learning methods in predicting the labels of the data samples. To our knowledge, this is the first time that LSTMs have been used for solar flare prediction.

Keywords: magnetic fields – methods: deep learning – Sun: activity – Sun: flares

1. INTRODUCTION

Solar flares, the largest explosive events in our solar system, are intense bursts of radiation that occur in the Sun's atmosphere and release massive amounts of energy into space. They last from minutes to hours and are often seen as bright chromospheric ribbons and hot coronal loops on the Sun. Some flares are small and innocent while others can be tremendous and violent. Powerful flares and the often accompanied coronal mass ejections (CMEs) can cause severe influences on the near-Earth environment, resulting in potentially life-threatening consequences (Daglis et al. 2004). Therefore, substantial efforts are being invested on solar flare research including forecast and mitigation plans.

The triggering mechanism of solar flares is far from being fully understood. Many studies have shown that flares and CMEs could be powered by the free magnetic energy accumulated in the coronal field, which can be impulsively released by magnetic reconnection (Priest & Forbes 2002; Shibata & Magara 2011). Since the buildup process of coronal free energy is driven by long-term evolution of the magnetic field on the photosphere (Takasao et al. 2015), the features of the photospheric magnetic field, which can be directly observed and derived from photospheric vector magnetograms, may be crucial indicators for the energy transportation and triggering processes of flares/CMEs. These features include the size and complexity of sunspots, unsigned magnetic flux, gradient of the magnetic field, magnetic energy dissipation, vertical electric currents, integrated Lorentz forces, magnetic shear, magnetic helicity injection, and so on (Park et al. 2008; Song et al. 2009; Yu et al. 2009; Steward et al. 2010). With the recent development of instruments and techniques, it becomes easier to obtain extensive measurements of these features.

Many researchers have demonstrated that using photospheric vector magnetograms in combination with machine learning can predict solar flares effectively. Bobra & Couvidat (2015) described 25 features, or predictive parameters, derived from vector magnetograms provided by the Helioseismic and Magnetic Imager (HMI; Schou et al. 2012) on board the *Solar Dynamics Observatory* (SDO; Pesnell et al. 2012). The authors considered flares of M1.0 class or

higher, as defined by the peak 1–8 Å flux measured by the *Geostationary Operational Environmental Satellite* system (*GOES*). Liu et al. (2017) took 13 parameters out of the 25 features and used them to perform multiclass predictions of solar flares. Nishizuka et al. (2017) employed both photospheric vector-magnetic field data and chromospheric data to predict prominent flares. The authors observed that pre-flare events such as ultraviolet brightening are associated with trigger mechanisms of solar flares. They counted the number of previous flares in an active region (AR) and showed that both the previous flare activity information and ultraviolet brightening are crucial for flare prediction. The authors later extended their study to include more features such as the X-ray intensity to further improve flare prediction performance (Nishizuka et al. 2018). Jonas et al. (2018) carried out solar flare prediction by utilizing photospheric vector-magnetic field data, flaring history, as well as multiple wavelengths of image data from the chromosphere, transition region, and corona. In contrast to the flare history used by Nishizuka et al. (2017, 2018), Jonas et al. (2018) constructed flare time series for each AR by taking the list of associated flares in the *GOES* solar-flare catalogs. The constructed time series are then convolved with exponentially decaying windows of varying length for flare prediction.

Machine learning is a subfield of artificial intelligence, which grants computers abilities to learn from the past data and make predictions on unseen future data (Alpaydin 2009). Commonly used machine learning methods for flare prediction include decision trees (Yu et al. 2009, 2010), random forests (Barnes et al. 2016; Liu et al. 2017; Florios et al. 2018; Breiman 2001), k-nearest neighbors (Li et al. 2008; Huang et al. 2013; Winter & Balasubramaniam 2015; Nishizuka et al. 2017), support vector machines (Qahwaji & Colak 2007; Yuan et al. 2010; Bobra & Couvidat 2015; Boucheron et al. 2015; Muranushi et al. 2015; Florios et al. 2018), ordinal logistic regression (Song et al. 2009), the least absolute shrinkage and selection operator (LASSO) (Benvenuto et al. 2018; Jonas et al. 2018), extremely randomized trees (Nishizuka et al. 2017), and neural networks (Qahwaji & Colak 2007; Wang et al. 2008; Colak & Qahwaji 2009; Higgins et al. 2011; Ahmed et al. 2013). Recently, Nishizuka et al. (2018) adopted a deep neural network, named Deep Flare Net, for flare prediction.

In this paper, we attempt to use *SDO*/HMI vector magnetic field data together with flaring history to predict solar flares that would occur in an AR within 24 hours of a given time point, with a deep learning method, named long short-term memory (LSTM) (Hochreiter & Schmidhuber 1997). An LSTM network is a special kind of recurrent neural networks (RNNs) (Hopfield 1982) that can learn the order dependence between samples in a sequence. LSTMs have been widely used in a variety of applications such as speech recognition (Graves & Schmidhuber 2005; Fernández et al. 2007; Graves et al. 2013), handwriting recognition (Graves et al. 2007; Graves & Schmidhuber 2008), time series forecasting (Schmidhuber et al. 2005) among others. In a solar flare prediction task, the observations in each AR form time series data, and hence LSTMs are suitable for this prediction task. To our knowledge, this is the first time that LSTMs are used for solar flare prediction.

The rest of this paper is organized as follows. Section 2 describes our data collection scheme and predictive parameters used in the study presented here. Section 3 details our LSTM architecture and algorithm. Section 4 reports experimental results. Section 5 concludes the paper.

2. DATA AND PREDICTIVE PARAMETERS

In this study we adopt the data product, named Space-weather HMI Active Region Patches (SHARP; Bobra et al. 2014), produced by the *SDO*/HMI team. These data were released at the end of 2012 (Bobra et al. 2014) and can be found as the `hmi.sharp` data series at the Joint Science Operations Center (JSOC).¹ The SHARP data encompass automatically identified and tracked ARs in map patches and provide many physical parameters suitable for flare prediction. Another useful data series, produced based on SHARP data, is `cgem.Lorentz`. This data series includes estimations of integrated Lorentz forces (Sun et al. 2014) which help diagnose the dynamic process of each AR (Fisher et al. 2012).

Our deep learning method requires training samples. We surveyed flares that occurred in the period between 2010 May and 2018 May, using the *GOES* X-ray flare catalogs provided by the National Centers for Environmental Information (NCEI), and selected flares with identified ARs in the NCEI flare catalogs. This yielded a database of 4,203 B-class flares, 6,768 C-class flares, 704 M-class flares, and 49 X-class flares. We used both the `hmi.sharp` data series and `cgem.Lorentz` data series, which were queried from the JSOC website by using SunPy (SunPy Community et al. 2015). The data samples were collected at a cadence of 1 hour.

¹ <http://jsoc.stanford.edu/>

We adopt two groups of predictive parameters for flare prediction. The first group contains the 25 physical parameters described in [Bobra & Couvidat \(2015\)](#) that characterize AR magnetic field properties. The second group contains 15 features related to flaring history. Six of the 15 features are related to time decay values and are calculated based on the formula described in [Jonas et al. \(2018\)](#). Specifically, for the data sample x_t observed at time point t in an AR, the time decay value of x_t with respect to B-class (C-class, M-class, X-class, respectively) flares, denoted $\text{Bdec}(x_t)$ ($\text{Cdec}(x_t)$, $\text{Mdec}(x_t)$, $\text{Xdec}(x_t)$, respectively), is computed respectively as

$$\text{Bdec}(x_t) = \sum_{f_i \in F_B} e^{-\frac{t-t(f_i)}{\tau}}, \quad (1)$$

$$\text{Cdec}(x_t) = \sum_{f_i \in F_C} e^{-\frac{t-t(f_i)}{\tau}}, \quad (2)$$

$$\text{Mdec}(x_t) = \sum_{f_i \in F_M} e^{-\frac{t-t(f_i)}{\tau}}, \quad (3)$$

$$\text{Xdec}(x_t) = \sum_{f_i \in F_X} e^{-\frac{t-t(f_i)}{\tau}}, \quad (4)$$

where F_B (F_C , F_M , F_X , respectively) represents the set of B-class (C-class, M-class, X-class, respectively) flares that occurred in the same AR before the data observation time point t , $t(f_i)$ denotes the occurrence time of flare f_i , and τ is a decay constant that is set to 12 as suggested by [Jonas et al. \(2018\)](#). Figure 1 illustrates how to calculate $\text{Mdec}(x_t)$ for a data sample x_t .

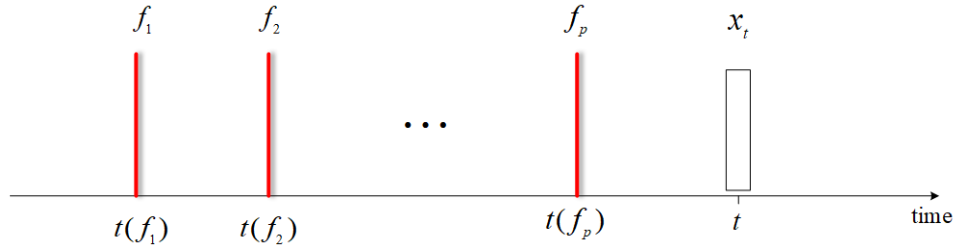


Figure 1. Calculation of the time decay value $\text{Mdec}(x_t)$ in an AR. The white rectangular box represents the data sample x_t observed and collected at time point t in the AR. There are p M-class flares that occurred in the same AR prior to time point t , so F_M contains p flares f_i , $1 \leq i \leq p$. Red vertical lines represent the occurrence times of the flares in F_M where the i th red vertical line indicates the starting time $t(f_i)$ of the i th M-class flare f_i .

The other two time decay values for the data sample x_t observed at time point t in an AR are computed by considering all flares, regardless of their classes, that occurred in the same AR before the time point t as follows:

$$\text{Edec}(x_t) = \sum_{f_i \in F} E(f_i) \cdot e^{-\frac{t-t(f_i)}{\tau}}, \quad (5)$$

$$\log\text{Edec}(x_t) = \sum_{f_i \in F} \log(E(f_i)) \cdot e^{-\frac{t-t(f_i)}{\tau}}, \quad (6)$$

where $F = F_B \cup F_C \cup F_M \cup F_X$ and $E(f_i)$ is the magnitude of flare f_i .

In addition, the second group contains 9 flare history features for the data sample x_t in the AR as described in [Nishizuka et al. \(2017\)](#). These nine features include Bhis (Chis , Mhis , Xhis , respectively) representing the total number of B-class (C-class, M-class, X-class, respectively) flares that occurred in the same AR before the data observation time point t , Bhis1d (Chis1d , Mhis1d , Xhis1d , respectively) representing the total number of B-class (C-class, M-class, X-class, respectively) flares that occurred in the same AR during the 24 hours (i.e., 1 day) prior to the time point t , and Xmax1d representing the maximum X-ray intensity in the same AR during the 24 hours prior to the time point t . In total, we use 40 features, including 25 physical features and 15 flare history features, which are summarized in Table 1.

Table 1. Overview of the 40 Features Including 25 *SDO*/HMI Magnetic Parameters and 15 Flare History Features

Keyword	Description	Formula
TOTUSJH	Total unsigned current helicity	$H_{c_{total}} \propto \sum B_z \cdot J_z $
TOTBSQ	Total magnitude of Lorentz force	$F \propto \sum B^2$
TOTPOT	Total photospheric magnetic free energy density	$\rho_{tot} \propto \sum (\mathbf{B}^{\text{Obs}} - \mathbf{B}^{\text{Pot}})^2 dA$
TOTUSJZ	Total unsigned vertical current	$J_{z_{total}} = \sum J_z dA$
ABSJZ	Absolute value of the net current helicity	$H_{c_{abs}} \propto \sum B_z \cdot J_z $
SAVNCPP	Sum of the modulus of the net current per polarity	$J_{z_{sum}} \propto \sum B_z^+ J_z dA + \sum B_z^- J_z dA $
USFLUX	Total unsigned flux	$\Phi = \sum B_z dA$
AREA_ACR	Area of strong field pixels in the active region	Area = \sum Pixels
MEANPOT	Mean photospheric magnetic free energy	$\bar{\rho} \propto \frac{1}{N} \sum (\mathbf{B}^{\text{Obs}} - \mathbf{B}^{\text{Pot}})^2$
R_VALUE	Sum of flux near polarity inversion line	$\Phi = \sum B_{LoS} dA$ within R mask
SHRGT45	Fraction of area with shear $> 45^\circ$	Area with shear $> 45^\circ$ / total area
MEANSHR	Mean shear angle	$\bar{\Gamma} = \frac{1}{N} \sum \arccos\left(\frac{\mathbf{B}^{\text{Obs}} \cdot \mathbf{B}^{\text{Pot}}}{ \mathbf{B}^{\text{Obs}} \mathbf{B}^{\text{Pot}} }\right)$
MEANGAM	Mean angle of field from radial	$\bar{\gamma} = \frac{1}{N} \sum \arctan\left(\frac{B_h}{B_z}\right)$
MEANGBT	Mean gradient of total field	$ \nabla B_{tot} = \frac{1}{N} \sum \sqrt{\left(\frac{\partial B}{\partial x}\right)^2 + \left(\frac{\partial B}{\partial y}\right)^2}$
MEANGBZ	Mean gradient of vertical field	$ \nabla B_z = \frac{1}{N} \sum \sqrt{\left(\frac{\partial B_z}{\partial x}\right)^2 + \left(\frac{\partial B_z}{\partial y}\right)^2}$
MEANGBH	Mean gradient of horizontal field	$ \nabla B_h = \frac{1}{N} \sum \sqrt{\left(\frac{\partial B_h}{\partial x}\right)^2 + \left(\frac{\partial B_h}{\partial y}\right)^2}$
MEANJZH	Mean current helicity	$\bar{H}_c \propto \frac{1}{N} \sum B_z J_z$
MEANJZD	Mean vertical current density	$\bar{J}_z \propto \frac{1}{N} \sum \left(\frac{\partial B_y}{\partial x} - \frac{\partial B_x}{\partial y}\right)$
MEANALP	Mean characteristic twist parameter, α	$\alpha_{total} \propto \frac{\sum J_z B_z}{\sum B_z^2}$
TOTFX	Sum of x -component of Lorentz force	$F_x \propto -\sum B_x B_z dA$
TOTFY	Sum of y -component of Lorentz force	$F_y \propto \sum B_y B_z dA$
TOTFZ	Sum of z -component of Lorentz force	$F_z \propto \sum (B_x^2 + B_y^2 - B_z^2) dA$
EPSX	Sum of x -component of normalized Lorentz force	$\delta F_x \propto \frac{\sum B_x B_z}{\sum B^2}$
EPSY	Sum of y -component of normalized Lorentz force	$\delta F_y \propto \frac{-\sum B_y B_z}{\sum B^2}$
EPSZ	Sum of z -component of normalized Lorentz force	$\delta F_z \propto \frac{\sum (B_x^2 + B_y^2 - B_z^2)}{\sum B^2}$
Bdec	Time decay value based on the previous B-class flares only	$Bdec(x_t) = \sum_{f_i \in F_B} e^{-\frac{t-t(f_i)}{\tau}}$
Cdec	Time decay value based on the previous C-class flares only	$Cdec(x_t) = \sum_{f_i \in F_C} e^{-\frac{t-t(f_i)}{\tau}}$
Mdec	Time decay value based on the previous M-class flares only	$Mdec(x_t) = \sum_{f_i \in F_M} e^{-\frac{t-t(f_i)}{\tau}}$
Xdec	Time decay value based on the previous X-class flares only	$Xdec(x_t) = \sum_{f_i \in F_X} e^{-\frac{t-t(f_i)}{\tau}}$
Edec	Time decay value based on the magnitudes of all previous flares	$Edec(x_t) = \sum_{f_i \in F} E_i \cdot e^{-\frac{t-t(f_i)}{\tau}}$
logEdec	Time decay value based on the log-magnitudes of all previous flares	$\log Edec(x_t) = \sum_{f_i \in F} \log(E_i) \cdot e^{-\frac{t-t(f_i)}{\tau}}$
Bhis	Total history of B-class flares in an AR	-
Chis	Total history of C-class flares in an AR	-
Mhis	Total history of M-class flares in an AR	-
Xhis	Total history of X-class flares in an AR	-
Bhis1d	1-day history of B-class flares in an AR	-
Chis1d	1-day history of C-class flares in an AR	-
Mhis1d	1-day history of M-class flares in an AR	-
Xhis1d	1-day history of X-class flares in an AR	-
Xmax1d	Maximum X-ray intensity one day before	-

Table 2. Numbers of Positive and Negative Samples for Each Flare Class

	$\geq C$ class		$\geq M$ class		$\geq M5.0$ class	
	Positive	Negative	Positive	Negative	Positive	Negative
Training	18,266	66,311	2,710	81,867	633	83,944
Validation	7,055	19,418	1,347	25,126	292	26,181
Testing	8,732	35,957	1,278	43,411	180	44,509

Because the features have different units and scales, we normalize the feature values as follows. For the 25 physical features, let z_i^k denote the normalized value of the i^{th} feature of the k^{th} data sample. Then

$$z_i^k = \frac{v_i^k - \mu_i}{\sigma_i}, \quad (7)$$

where v_i^k is the original value of the i^{th} feature of the k^{th} data sample, μ_i is the mean of the i^{th} feature, and σ_i is the standard deviation of the i^{th} feature. For the 15 flare history features, we have

$$z_i^k = \frac{v_i^k - \min_i}{\max_i - \min_i}, \quad (8)$$

where \max_i and \min_i are the maximum and minimum value of the i^{th} feature, respectively.

3. METHODOLOGY

3.1. Prediction Task

Following Bobra & Couvidat (2015), Jonas et al. (2018) and Nishizuka et al. (2018), we intend to use past observations of an AR to predict its future flaring activity. Specifically, we want to solve the following binary classification problem: will this AR produce a Υ -class flare within the next 24 hours? We consider three Υ classes separately: $\geq M5.0$ class, $\geq M$ class, and $\geq C$ class. The importance of these classes has been discussed in recent works (Jonas et al. 2018; Nishizuka et al. 2018). Both the $\geq M$ class and $\geq C$ class were studied in Nishizuka et al. (2018). Also, the $\geq M$ class was discussed in Liu et al. (2017) and the $\geq C$ class was analyzed in Jonas et al. (2018). In addition, we consider the $\geq M5.0$ class due to the few X-class flares in our dataset where a $\geq M5.0$ -class flare means the *GOES* X-ray flux value of the flare is above $5 \times 10^{-5} \text{Wm}^{-2}$. A flare in the $\geq M5.0$ class is generally considered a major flare.

As in Bobra & Couvidat (2015), observation data whose AR is outside $\pm 70^\circ$ of the center meridian or whose features are incomplete are ignored. Data samples collected in years 2010–2013 are used for training, those in year 2014 are used for validation, and those in years 2015–2018 are used for testing. The training set and testing set are disjoint, and hence our algorithm will make predictions on ARs that it has never seen before. Figure 2 illustrates how we construct positive samples and negative samples used by the proposed deep learning method. For the $\geq C$ class, data samples collected 24 hours prior to an X-class, M-class, or C-class flare in an AR are positive and all other data samples in the AR are negative. For the $\geq M$ class, data samples collected 24 hours prior to an X-class or M-class flare in an AR are positive and all other data samples in the AR are negative. For the $\geq M5.0$ class, data samples collected 24 hours prior to a $\geq M5.0$ -class flare in an AR are positive and all other data samples in the AR are negative. Notice that, if a data sample is missing at some time point or if there are insufficient data samples during the 24 hours prior to a Υ -class flare, we adopt a zero-padding strategy by adding synthetic data samples with zeros for all feature values to yield a complete non-gapped time-series dataset. This zero-padding method is used after applying the normalization procedures described in Equations (7) and (8). Therefore, the zero-padding method does not affect the normalization procedures. Table 2 shows the numbers of positive and negative samples for each flare class where there are 1,269 ARs in total. Because most ARs do not produce flares, our approach yields an imbalanced dataset in which negative samples greatly outnumber positive samples.

For a given time point t and an AR, the proposed deep learning method predicts whether the AR will produce a Υ -class flare within the next 24 hours of t . There are three Υ classes, namely $\geq M5.0$ class, $\geq M$ class, and $\geq C$ class. Therefore, we build three deep learning models separately, referred to as the $\geq M5.0$ model, $\geq M$ model, and $\geq C$ model respectively, each corresponding to a Υ class of flares.

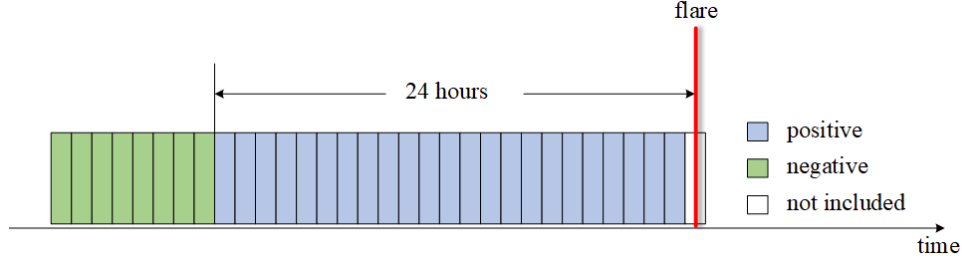


Figure 2. Construction of positive and negative samples used in the prediction task. Each rectangular box represents a data sample, and corresponds to 1 hour in time. The red vertical line indicates the starting time of a Υ -class flare. Data samples collected 24 hours prior to the flare, represented by blue rectangular boxes, belong to the positive class. The other data samples, represented by green rectangular boxes, belong to the negative class. The white rectangular box, in which the flare occurs, is not included in our dataset.

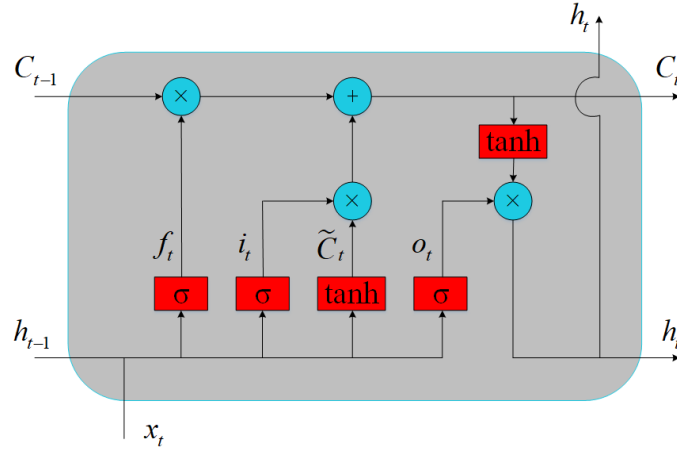


Figure 3. Illustration of an LSTM unit. Here, f_t is the forget gate, i_t is the input gate, o_t is the output gate, C_t is the cell state, x_t is the input vector to the LSTM unit, and h_t is the output vector of the LSTM unit.

3.2. Prediction Method

Our deep learning models employ a long short-term memory (LSTM) network. An LSTM unit contains four interactive parts including a memory cell, an input gate, an output gate and a forget gate, as illustrated in Figure 3. The key to LSTMs is the cell state, which is represented by the horizontal line at the top of the diagram in Figure 3. Specifically, the new cell state C_t is updated by the old cell state C_{t-1} and the candidate cell state \tilde{C}_t as follows:

$$C_t = f_t \odot C_{t-1} + i_t \odot \tilde{C}_t, \quad (9)$$

where the forget gate f_t that controls the extent to which a value remains in the cell is calculated as:

$$f_t = \sigma(W_f \cdot [h_{t-1}, x_t] + B_f), \quad (10)$$

and the input gate i_t that controls the extent to which a new value flows into the cell is computed as:

$$i_t = \sigma(W_i \cdot [h_{t-1}, x_t] + B_i). \quad (11)$$

Here x_t represents the input vector at time step t and h_{t-1} represents the output vector at time step $t-1$. The candidate cell state \tilde{C}_t is computed as:

$$\tilde{C}_t = \tanh(W_c \cdot [h_{t-1}, x_t] + B_c). \quad (12)$$

Finally, the output vector h_t at time step t , which is based on the new cell state C_t , is computed as:

$$h_t = o_t \odot \tanh(C_t), \quad (13)$$

where

$$o_t = \sigma(W_o \cdot [h_{t-1}, x_t] + B_o). \quad (14)$$

In the above equations, W and B contain weights and biases respectively, which need to be learned during training; $[\cdot]$ denotes the concatenation of two vectors; $\sigma(\cdot)$ is the sigmoid function, i.e., $\sigma(z) = \frac{1}{1+e^{-z}}$; $\tanh(\cdot)$ is the hyperbolic tangent function, i.e., $\tanh(z) = \frac{e^z - e^{-z}}{e^z + e^{-z}}$; \odot denotes the Hadamard product (element-wise multiplication).

Our deep learning architecture contains an LSTM layer with m LSTM units (in the study presented here, m is set to 10). Motivated by the previous work in language translation (Bahdanau et al. 2014), where attention mechanism was applied to allow a model to automatically search for parts of a source sentence that are related to the prediction of a target word, we add an attention layer with m neurons above the LSTM layer to focus on information in relevant time steps. The attention layer would take the states in all time steps into account and assign a weight to each state, which indicates the importance of information that state has. The weight w_i for state h_i is derived by comparing the target state with each source state, which is computed as:

$$w_i = \frac{e^{\text{score}(h_i, h_t)}}{\sum_j e^{\text{score}(h_j, h_t)}}. \quad (15)$$

Here, h_t is the state at the last time step and $\text{score}(\cdot)$ is a content-based function. We adopt the function used by Luong et al. (2015), which is defined as

$$\text{score}(h_i, h_t) = h_t^T W h_i, \quad (16)$$

where W contains learnable parameters. After w_i is obtained, a context vector c_t can be computed as:

$$c_t = \sum_i w_i h_i. \quad (17)$$

The final attention vector v of the input sequence is derived by concatenating the context vector c_t and last hidden state h_t , and then being activated by a hyperbolic tangent layer as follows:

$$v = \tanh(W_v [c_t; h_t]). \quad (18)$$

This activation vector v is then sent to two fully connected layers, the first one having 200 neurons and the second one having 500 neurons. Finally the output layer with 2 neurons, which is activated by the softmax function, produces predicted values. Figure 4 shows the overall architecture of our LSTM network.

Let x_t represent the data sample collected at time point t . During training, for each time point t , we take m consecutive data samples $x_{t-m+1}, x_{t-m+2}, \dots, x_{t-1}, x_t$ from the training set and use the m consecutive data samples to train the LSTM network. The label of these m consecutive data samples is defined to be the label of the last data sample x_t . Thus, if x_t belongs to the positive class, then the input sequence $x_{t-m+1}, x_{t-m+2}, \dots, x_{t-1}, x_t$ is defined as positive; otherwise the sequence is defined as negative. Because the data samples are collected continuously at a cadence of 1 hour and missing values are filled up by our zero-padding strategy, the input sequence spans m hours.

Because the dataset at hand is imbalanced where negative samples outnumber positive samples (see Table 2), we use a weighted cross entropy cost function for optimizing model parameters during training. The cost function is computed as:

$$J = \sum_{n=1}^N \sum_{k=1}^K \omega_k y_{nk} \log(\hat{y}_{nk}). \quad (19)$$

Here, N is the total number of sequences each having m consecutive data samples in the training set, K is the number of classes, which is 2 in our case since we have only positive and negative classes, ω_k is the weight of the k th class, which is derived by the ratio of the sizes of the positive and negative classes with more weight given to the minority (i.e., positive) class, y_{nk} and \hat{y}_{nk} denote the observed probability (which is equal to 1 if the n th sequence belongs to the k th class) and the estimated probability of being in the k th class of the n th sequence, respectively.²

² We model data samples in ARs as time series. However, we do not bind the many time series to a single one. Instead, we process ARs separately as follows. Our LSTM network accepts as input $m=10$ data samples at a time. Assuming there are P data samples on an active region $AR1$, with our zero-padding strategy, we generate P sequences each having 10 data samples from $AR1$, and feed these P sequences, one sequence at a time, to the LSTM network. Next, assuming there are Q data samples on another active region $AR2$, we generate Q sequences each having 10 data samples from $AR2$, and feed these Q sequences, one sequence at a time, to the LSTM network. Although $AR1$ and $AR2$ may have overlapping time points, we process the active regions separately, one at a time. N in Equation (19) represents the total number of sequences we generate from the training set.

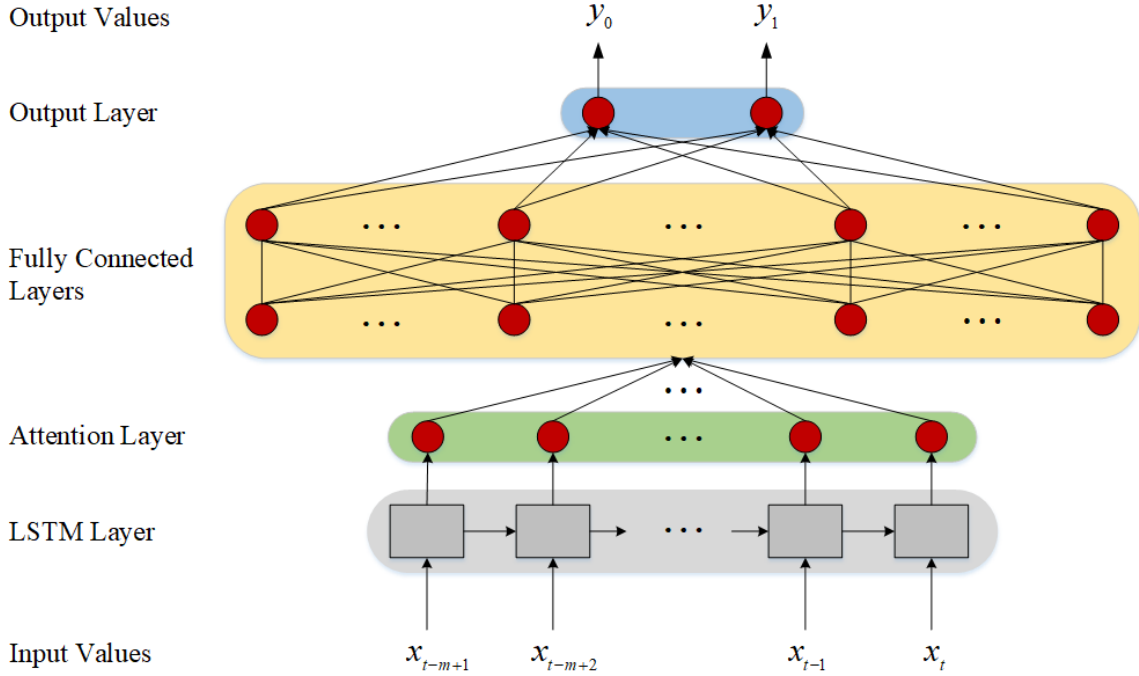


Figure 4. Architecture of the proposed LSTM network. This network is mainly comprised of an LSTM layer, an attention layer, two fully connected layers and an output layer. Each gray box in the LSTM layer is an LSTM unit as shown in Figure 3. There are m LSTM units in the LSTM layer, m neurons in the attention layer, 200 neurons in the first fully connected layer, 500 neurons in the second fully connected layer, and 2 neurons in the output layer activated by the softmax function. The LSTM network takes as input the sequence $x_{t-m+1}, x_{t-m+2}, \dots, x_{t-1}, x_t$ and produces as output a 2-dimension vector $[y_0, y_1]$ with a value of $[1, 0]$ or $[0, 1]$ which is determined by the probability calculated by the softmax function in the output layer.

The proposed LSTM network is implemented in Python, TensorFlow and Keras. A mini-batch strategy (Goodfellow et al. 2016) is used to achieve faster convergence during backpropagation. The validation dataset is used for tuning model hyperparameters. The optimizer used is Adam (Kingma & Ba 2014), which is a method for stochastic gradient descent, where the learning rate is set to 0.001, β_1 is set to 0.9, and β_2 is set to 0.999. The batch size is set to 256 and the number of epochs is set to 7. The length of each input sequence, m , is set to 10, meaning that every time 10 consecutive data samples are used as input to our LSTM network.

During testing, to predict whether an AR will produce a Υ -class flare within the next 24 hours of a time point t , we take x_t and its preceding $m - 1$ data samples, and then feed the m consecutive testing data samples $x_{t-m+1}, x_{t-m+2}, \dots, x_{t-1}, x_t$ into the trained LSTM network. Here, the Υ class refers to the $\geq M5.0$ class, $\geq M$ class, and $\geq C$ class, respectively. The output of the LSTM network, i.e., the predicted result, is a 2-dimension vector $[y_0, y_1]$ with a value of $[1, 0]$ or $[0, 1]$, indicating x_t is positive (i.e., the AR will produce a Υ -class flare within the next 24 hours of t) or x_t is negative (i.e., the AR will not produce a Υ -class flare within the next 24 hours of t). This value is determined by comparing the probability calculated by the softmax function with a threshold. If the probability is greater than or equal to the threshold, then x_t is predicted to be positive; otherwise x_t is predicted to be negative. It should be pointed out that, the way we use the m consecutive testing data samples $x_{t-m+1}, x_{t-m+2}, \dots, x_{t-1}, x_t$ to predict whether there is a $\geq M5.0$ -class ($\geq M$ -class, $\geq C$ -class, respectively) flare within the next 24 hours of the time point t is totally different from the previously published machine learning methods for solar flare prediction (Bobra & Couvidat 2015; Jonas et al. 2018; Nishizuka et al. 2018), which used only the testing data sample x_t to make the prediction.

4. RESULTS

4.1. Performance Metrics

Given an AR and a data sample x_t observed at time point t , we define x_t to be a true positive (TP) if the $\geq M5.0$ ($\geq M$, $\geq C$, respectively) model predicts that x_t is positive, i.e., the AR will produce a $\geq M5.0$ - ($\geq M$ -, $\geq C$ -, respectively)

class flare within the next 24 hours of t , and x_t is indeed positive. We define x_t to be a false positive (FP) if the $\geq M5.0$ ($\geq M$, $\geq C$, respectively) model predicts that x_t is positive while x_t is actually negative i.e., the AR will not produce a $\geq M5.0$ - ($\geq M$ -, $\geq C$ -, respectively) class flare within the next 24 hours of t . We say x_t is a true negative (TN) if the $\geq M5.0$ ($\geq M$, $\geq C$, respectively) model predicts x_t to be negative and x_t is indeed negative; x_t is a false negative (FN) if the $\geq M5.0$ ($\geq M$, $\geq C$, respectively) model predicts x_t to be negative while x_t is actually positive. We also use TP (FP, TN, FN, respectively) to represent the total number of true positives (false positives, true negatives, false negatives, respectively) produced by a model.

The performance metrics used in this study include the following:

$$\text{Recall} = \frac{\text{TP}}{\text{TP} + \text{FN}}, \quad (20)$$

$$\text{Precision} = \frac{\text{TP}}{\text{TP} + \text{FP}}, \quad (21)$$

$$\text{Accuracy (ACC)} = \frac{\text{TP} + \text{TN}}{\text{TP} + \text{FP} + \text{TN} + \text{FN}}, \quad (22)$$

$$\text{Balanced Accuracy (BACC)} = \frac{1}{2} \left(\frac{\text{TP}}{\text{TP} + \text{FN}} + \frac{\text{TN}}{\text{TN} + \text{FP}} \right), \quad (23)$$

$$\text{Heidke Skill Score (HSS)} = \frac{2(\text{TP} \times \text{TN} - \text{FP} \times \text{FN})}{(\text{TP} + \text{FN})(\text{FN} + \text{TN}) + (\text{TP} + \text{FP})(\text{FP} + \text{TN})}, \quad (24)$$

$$\text{True Skill Statistics (TSS)} = \frac{\text{TP}}{\text{TP} + \text{FN}} - \frac{\text{FP}}{\text{TN} + \text{FP}}. \quad (25)$$

ACC is not suitable for imbalanced classification (He & Garcia 2009). The reason is that a naive classifier predicting all instances in the minority class to belong to the majority class would still get a high ACC value. Instead, BACC is suggested for imbalanced classification (He & Garcia 2009). Because of its unbiasedness over class-imbalance ratios, we also follow the suggestion of Bloomfield et al. (2012) to use the TSS score, which is the recall subtracted by the false alarm rate. The Heidke Skill Score (HSS) (Heidke 1926) is used to measure the fractional improvement of our prediction over the random prediction (Florios et al. 2018). The larger BACC, HSS, and TSS score a method has, the better performance the method achieves.

4.2. Model Evaluation

We first conduct an ablation study to analyze the proposed LSTM framework by considering three alternative architectures, denoted by LSTM_{-a}, LSTM_{-c} and LSTM_{-ac}, respectively. LSTM_{-a} (LSTM_{-c}, LSTM_{-ac}, respectively) is obtained by removing the attention layer (the two fully connected layers, both the attention layer and the two fully connected layers, respectively) from the LSTM architecture in Figure 4. Table 3 shows the prediction results of the four architectures for the three Υ classes, namely $\geq M5.0$ class, $\geq M$ class, and $\geq C$ class, of flares. It can be seen from Table 3 that the proposed LSTM architecture outperforms the ablations LSTM_{-a}, LSTM_{-c} and LSTM_{-ac} in terms of BACC, HSS and TSS scores. By including the attention layer and the two fully connected layers, the performance of the LSTM framework improves. Our zero-padding strategy does not negatively affect the prediction performance. Although *some* normalized feature values of a data sample may become zeros due to the normalization procedures described in Equations (7) and (8), the attention layer of our LSTM model is able to distinguish between this data sample and those synthetic data samples added by our zero-padding method whose feature values are *all* zeros. The attention layer pays little attention to the synthetic data samples whose feature values are all zeros.

We next compare our LSTM framework with five closely related machine learning methods including multilayer perceptrons (MLP) (Haykin & Network 2004; Florios et al. 2018), Jordan network (JN) (Jordan 1997), support vector machines (SVM) (Qahwaji & Colak 2007; Yuan et al. 2010; Bobra & Couvidat 2015; Boucheron et al. 2015; Muranushi et al. 2015; Florios et al. 2018), random forests (RF) (Barnes et al. 2016; Liu et al. 2017; Florios et al. 2018), and a recently published deep learning-based method, Deep Flare Net (DeFN; Nishizuka et al. 2018). All these methods including ours (LSTM) can be used as a binary classification model (Nishizuka et al. 2018; Jonas et al. 2018) or a probabilistic forecasting model (Florios et al. 2018). A binary classification model predicts whether or not an AR will

Table 3. Flare Prediction Results (within 24 hours) of Four LSTM Architectures

		$\geq M5.0$ class	$\geq M$ class	$\geq C$ class
Recall	LSTM _{-ac}	0.944	0.888	0.743
	LSTM _{-a}	0.939	0.899	0.747
	LSTM _{-c}	0.956	0.876	0.750
	LSTM	0.978	0.881	0.762
Precision	LSTM _{-ac}	0.042	0.181	0.543
	LSTM _{-a}	0.039	0.184	0.537
	LSTM _{-c}	0.041	0.216	0.536
	LSTM	0.038	0.222	0.544
ACC	LSTM _{-ac}	0.914	0.882	0.828
	LSTM _{-a}	0.904	0.883	0.825
	LSTM _{-c}	0.910	0.906	0.824
	LSTM	0.899	0.909	0.829
BACC	LSTM _{-ac}	0.929	0.885	0.796
	LSTM _{-a}	0.933	0.891	0.795
	LSTM _{-c}	0.933	0.891	0.796
	LSTM	0.938	0.895	0.803
HSS	LSTM _{-ac}	0.074	0.267	0.519
	LSTM _{-a}	0.068	0.271	0.515
	LSTM _{-c}	0.071	0.316	0.514
	LSTM	0.074	0.347	0.539
TSS	LSTM _{-ac}	0.858	0.770	0.591
	LSTM _{-a}	0.865	0.782	0.591
	LSTM _{-c}	0.865	0.783	0.592
	LSTM	0.877	0.790	0.607

produce a $\geq M5.0$ - ($\geq M$ -, $\geq C$ -, respectively) class flare within the next 24 hours. A probabilistic forecasting model predicts the probability for an AR to produce a $\geq M5.0$ - ($\geq M$ -, $\geq C$ -, respectively) class flare within the next 24 hours. A probabilistic forecasting model can be converted into a binary classification model by using a probability threshold to make predictions as follows. If the predicted probability is greater than or equal to the threshold, then the AR will produce a flare within the next 24 hours; otherwise the AR will not produce a flare within the next 24 hours.

The MLP method consists of an input layer, an output layer and two hidden layers with 200 neurons and 500 neurons respectively. For the JN method, its output dimension is set to 10. SVM uses the radial basis function (RBF) kernel. RF has two parameters: mtry (number of features randomly selected to split a node) and ntree (number of trees to grow in the forest). We vary the values of ntree $\in \{300, 500, 1,000\}$ and mtry $\in [2, 8]$, and set ntree to 500 and mtry to 3 since these two parameter values yield the maximum TSS for RF. Table 4 compares our LSTM with the five related methods. All the methods are treated as binary classification models where the probability thresholds are chosen to maximize their respective TSS values, and the same threshold is used to calculate all performance metrics including BACC, HSS and TSS for each method with respect to each flare class. It can be seen from Table 4 that LSTM and RF are the two best methods. The probability thresholds used by LSTM in Table 4 are 50%, 60% and 50% for $\geq M5.0$, $\geq M$ and $\geq C$ models respectively (the same thresholds are used in Table 3). The probability thresholds used by RF in Table 4 are 0.5%, 5% and 25% for $\geq M5.0$, $\geq M$ and $\geq C$ models respectively.

To further understand the behavior of the proposed LSTM method, we conduct a cross-validation study as follows. Refer to Table 2. For each of the $\geq M5.0$, $\geq M$ and $\geq C$ models, we partition its training (testing, respectively) set into 10 equal-sized folds. For every two training (testing, respectively) folds i and j , $i \neq j$, fold i and fold j are disjoint; furthermore, fold i and fold j contain approximately the same number of positive training (testing, respectively) data samples and approximately the same number of negative training (testing, respectively) data samples. In run (i, j) , $1 \leq i \leq 10$, $1 \leq j \leq 10$, all training samples except those in training fold i are used to train a model, and the trained model is used to make predictions on all testing samples except those in testing fold j . We calculate the performance

Table 4. Flare Prediction Results (within 24 hours) of Our LSTM and Five Related Machine Learning Methods

		$\geq M5.0$ class	$\geq M$ class	$\geq C$ class
Recall	MLP	0.944	0.812	0.637
	SVM	0.644	0.692	0.746
	JN	0.923	0.851	0.701
	DeFN	0.889	0.891	0.761
	RF	1.000	0.850	0.727
	LSTM	0.978	0.881	0.762
Precision	MLP	0.037	0.143	0.451
	SVM	0.014	0.106	0.497
	JN	0.033	0.178	0.543
	DeFN	0.037	0.173	0.497
	RF	0.034	0.252	0.532
	LSTM	0.038	0.222	0.544
ACC	MLP	0.901	0.855	0.778
	SVM	0.818	0.824	0.803
	JN	0.882	0.884	0.826
	DeFN	0.907	0.872	0.801
	RF	0.886	0.924	0.822
	LSTM	0.899	0.909	0.829
BACC	MLP	0.922	0.834	0.725
	SVM	0.732	0.760	0.781
	JN	0.903	0.868	0.779
	DeFN	0.898	0.881	0.786
	RF	0.943	0.888	0.786
	LSTM	0.938	0.895	0.803
HSS	MLP	0.064	0.204	0.389
	SVM	0.020	0.141	0.472
	JN	0.056	0.260	0.502
	DeFN	0.064	0.253	0.476
	RF	0.059	0.361	0.502
	LSTM	0.074	0.347	0.539
TSS	MLP	0.845	0.669	0.449
	SVM	0.464	0.520	0.562
	JN	0.806	0.736	0.558
	DeFN	0.796	0.763	0.572
	RF	0.886	0.776	0.572
	LSTM	0.877	0.790	0.607

metric values based on the predictions made in run (i, j) . There are 100 runs. The means and standard deviations over the 100 runs are calculated and recorded.

4.3. Feature Assessment

Motivated by RF which uses only 3 features to split a node when constructing a tree, we wonder whether using fewer features can also achieve better performance for our LSTM method. We thus analyze the importance of each of the 40 features studied in the paper with respect to the $\geq M5.0$, $\geq M$, and $\geq C$ models respectively based on the LSTM architecture in Figure 4 using the cross-validation methodology described above. Each time only one feature is used by the $\geq M5.0$ ($\geq M$, $\geq C$, respectively) model to predict whether a given AR will produce a $\geq M5.0$ - ($\geq M$ -, $\geq C$ -, respectively) class flare within the next 24 hours. The probability threshold is set to maximize the TSS score in each test. The corresponding mean TSS score is recorded. There are 40 features, so 40 mean individual TSS scores

are recorded. These 40 mean individual TSS scores are sorted in descending order, and the 40 corresponding features are ranked from the most important to the least important accordingly. The sorted, mean individual TSS scores and ranked features are plotted in a chart for each model. Then, according to the ranked features, mean cumulative TSS scores are calculated and plotted in the chart. Specifically, the mean cumulative TSS score of the top k , $1 \leq k \leq 40$, most important features with respect to the $\geq M5.0$ ($\geq M$, $\geq C$, respectively) model is equal to the mean TSS score of the $\geq M5.0$ ($\geq M$, $\geq C$, respectively) model that uses the top k most important features altogether for flare prediction.

Figure 5 (6, 7, respectively) presents the feature importance chart for the $\geq M5.0$ ($\geq M$, $\geq C$, respectively) model. In each figure, blue bars represent mean individual TSS scores of the 40 features and the red polygonal line represents mean cumulative TSS scores of the top k , $1 \leq k \leq 40$, most important features. Error bars, representing standard deviations, are also plotted. It can be seen from the figures that predictive parameters that are consistently ranked in the top 20 list for all the three models include the following 16 features: TOTUSJH, TOTBSQ, TOTPOT, TOTUSJZ, ABSNJZH, SAVNCP, USFLUX, AREA_ACR, MEANPOT, TOTFX, Cdec, Chis, Chis1d, Edec, Mhis and Xmax1d. Among these 16 features, there are 10 physical parameters, or *SDO*/HMI magnetic parameters, including TOTUSJH, TOTBSQ, TOTPOT, TOTUSJZ, ABSNJZH, SAVNCP, USFLUX, AREA_ACR, MEANPOT and TOTFX. All these 10 physical parameters except TOTFX are among the 13 magnetic parameters that are also considered important in Bobra & Couvidat (2015) and Liu et al. (2017), which used different methods for assessing the importance of features. Thus, our findings are consistent with those reported in the literature. There are 4 magnetic parameters, TOTFZ, R_VALUE, SHRGT45 and EPSZ, which are considered important in Bobra & Couvidat (2015) and Liu et al. (2017), but are not ranked high in our list; some flare history features are ranked higher than these four magnetic parameters. It is worth noting that TOTUSJH plays the most important role, i.e., is ranked the top one, for all the three models. Moreover, some features including TOTUSJH, TOTUSJZ, TOTPOT, TOTBSQ, USFLUX, SAVNCP, Cdec, Chis and Chis1d show strong predictive power and are consistently ranked in the top 10 list for all the three models.

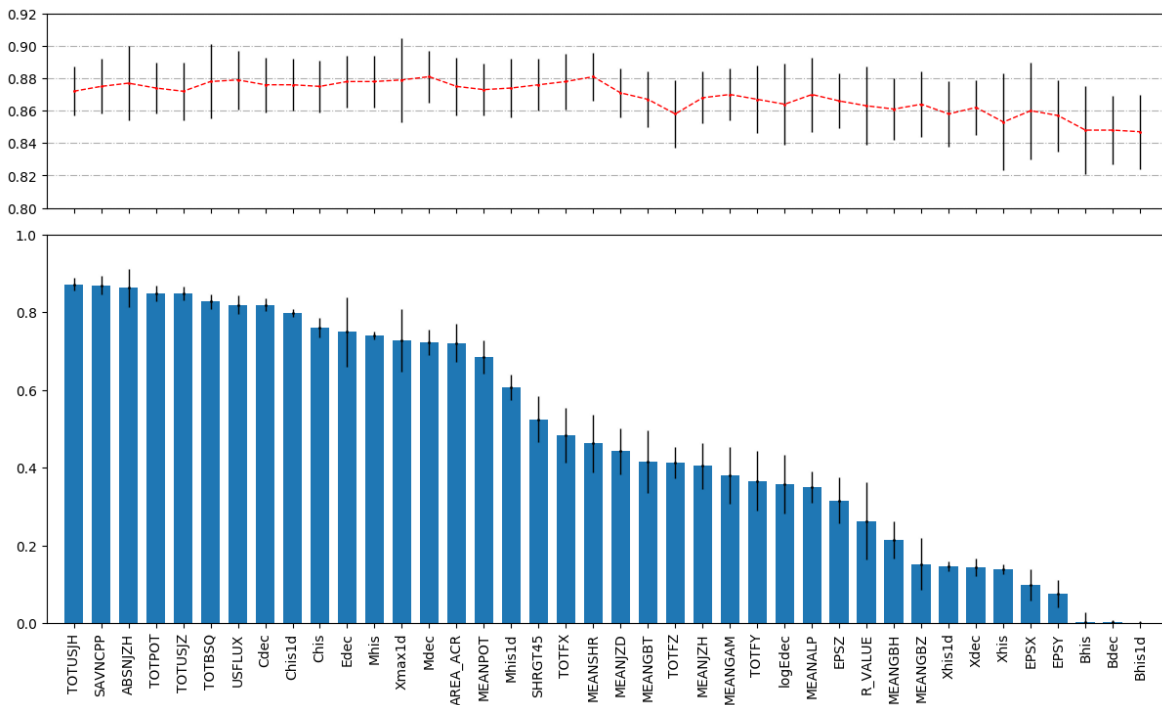


Figure 5. Assessment of feature importance for predicting $\geq M5.0$ -class flares. Blue bars represent mean individual TSS scores and the red polygonal line represents mean cumulative TSS scores of the features.

We note that the history of C-class flares has a high impact on flare prediction. Chis and Chis1d from Nishizuka et al. (2017) count the number of previous C-class flares. Cdec from Jonas et al. (2018) is the time decay value based on previous C-class flares. These three flare history features are ranked high in our list. The history of M-class flares plays a more important role for the $\geq M5.0$ and $\geq M$ models than for the $\geq C$ model. Other flare history features such

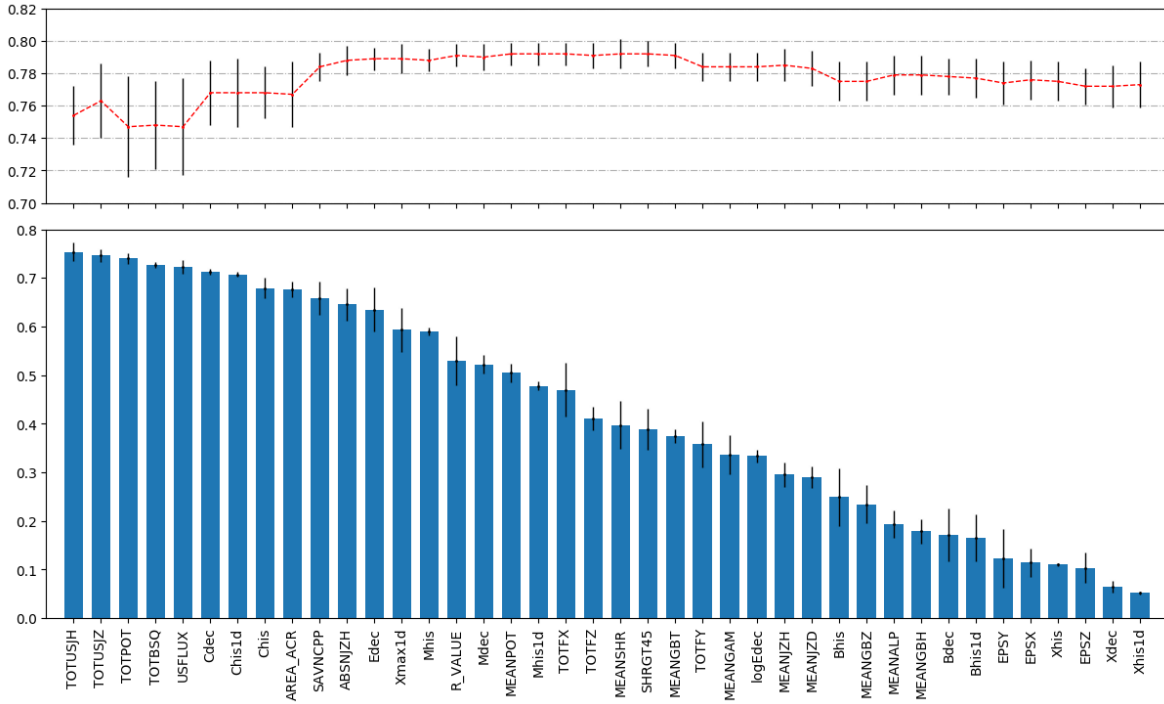


Figure 6. Assessment of feature importance for predicting $\geq M$ -class flares. Blue bars represent mean individual TSS scores and the red polygonal line represents mean cumulative TSS scores of the features.

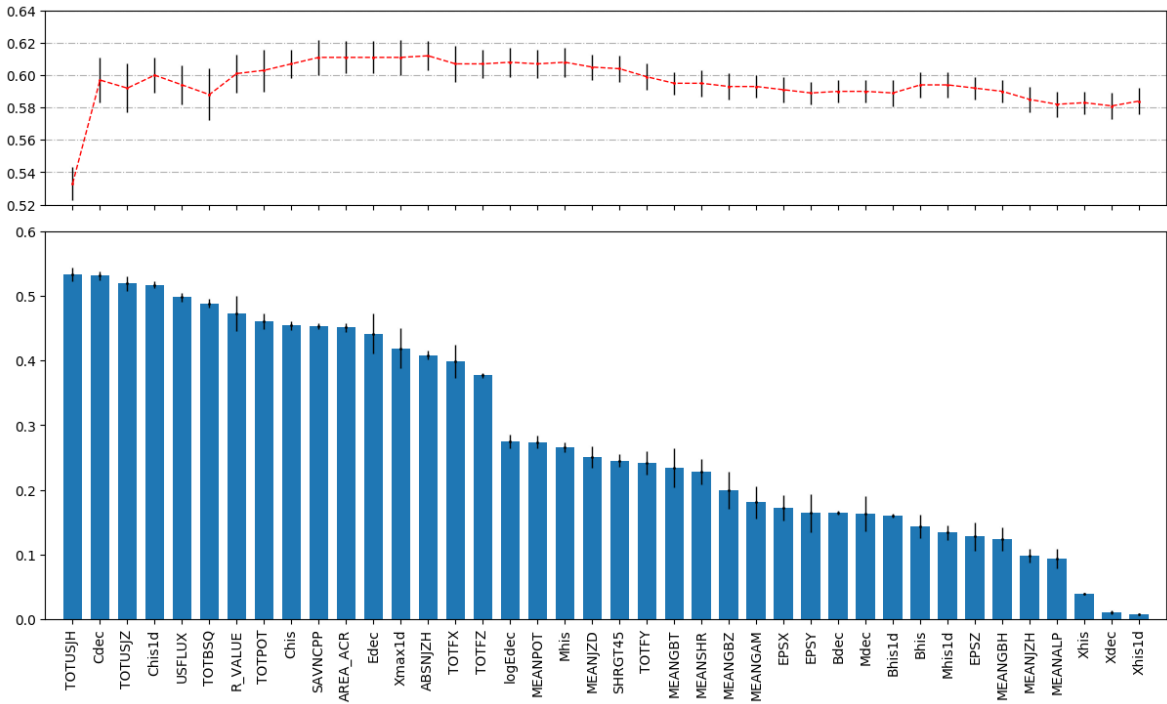


Figure 7. Assessment of feature importance for predicting $\geq C$ -class flares. Blue bars represent mean individual TSS scores and the red polygonal line represents mean cumulative TSS scores of the features.

Table 5. Flare Prediction Results (within 24 hours) of Our LSTM and RF Obtained from Cross Validation

		$\geq M5.0$ class	$\geq M$ class	$\geq C$ class
Recall	RF	0.960 (0.027)	0.888 (0.006)	0.730 (0.002)
	LSTM	0.960 (0.017)	0.885 (0.017)	0.773 (0.027)
Precision	RF	0.026 (0.001)	0.179 (0.003)	0.499 (0.003)
	LSTM	0.048 (0.008)	0.222 (0.023)	0.541 (0.030)
ACC	RF	0.853 (0.003)	0.880 (0.002)	0.804 (0.001)
	LSTM	0.921 (0.014)	0.907 (0.013)	0.826 (0.015)
BACC	RF	0.906 (0.014)	0.884 (0.003)	0.776 (0.001)
	LSTM	0.940 (0.007)	0.896 (0.004)	0.806 (0.004)
HSS	RF	0.042 (0.002)	0.262 (0.004)	0.469 (0.003)
	LSTM	0.084 (0.015)	0.323 (0.030)	0.526 (0.021)
TSS	RF	0.812 (0.027)	0.768 (0.005)	0.552 (0.003)
	LSTM	0.881 (0.014)	0.792 (0.008)	0.612 (0.009)

as the histories of B-class and X-class flares are relatively unimportant for predicting $\geq M5.0$ - ($\geq M$ -, $\geq C$ -, respectively) class flares.

By carefully examining Figures 5, 6 and 7, we find that using all the 40 features together does not yield the highest mean cumulative TSS scores. In fact, using roughly the top 14-22 most important features together yields the highest mean cumulative TSS scores, achieving the best performance. Specifically, using the top 20 (22, 14, respectively) most important features yields the highest mean cumulative TSS score for the $\geq M5.0$ ($\geq M$ -, $\geq C$ -, respectively) model. This happens probably because low ranked features are noisy features, and using them may deteriorate the performance of the models. In subsequent experiments, we use the best features for each model.

4.4. Comparison between RF and LSTM

Table 4 shows that RF and LSTM are the two best methods. In this subsection, we further compare RF and LSTM using the cross-validation methodology described above. Table 5 shows their performance metric values where standard deviations are enclosed in parentheses. The probability thresholds used by RF are set to 0.5%, 5%, 25% for $\geq M5.0$, $\geq M$ -, $\geq C$ - class respectively where the thresholds are chosen to maximize TSS. The probability thresholds used by LSTM are set to 75%, 60%, 50% for $\geq M5.0$, $\geq M$ -, $\geq C$ - class respectively. These optimal thresholds are slightly different from those used in Table 4. This happens because the performance metric values in Table 4 are obtained from a single dataset whereas those in Table 5 are obtained from cross validation. Furthermore, LSTM in Table 4 uses all 40 features together whereas LSTM in Table 5 uses only the (14-22) best features. According to Table 5 and a Wilcoxon signed rank test (Wilcoxon 1947), our LSTM method is significantly better than RF ($p < 0.05$) in all three flare classes in terms of BACC, HSS and TSS.³ These results indicate that LSTM outperforms RF when the methods are used as binary classification models.

We next compare RF and LSTM using (i) skill scores profiles (SSP) of BACC, HSS and TSS as functions of the probability threshold, (ii) Receiver Operating Characteristic (ROC) curves, and (iii) Reliability Diagrams (RD). ROC curves describe the relationship between the true positive rate and false positive rate. The Area Under the Curve (AUC) in the ROC represents the degree of separability, indicating how well a model is capable of distinguishing between two classes with the ideal value of one (Marzban 2004). The RD describes the relationship between the actual observed frequencies of flares of interest and the probabilities predicted by a model. A bin diagram, presented as an inset in the RD, is used to show the distribution of the predicted probabilities. The X-axis of the bin diagram represents the predicted probabilities and the Y-axis represents the numbers of data samples. As in Florios et al. (2018) we use 20 bins of length 0.05 each. Thus, for example, the Y value of the first bin shows the number of data samples whose predicted probabilities of having a flare of interest in the next 24 hours are within 0.05. The ideal situation is represented by the diagonal line in the RD; a point (x, x) on the diagonal indicates that among those data samples whose predicted probability is x , the ratio of the data samples that actually have a flare of interest within the next 24 hours is also x . In addition, we use the Brier Score (BS) (Brier 1950) and Brier Skill Score (BSS) (Wilks

³ The source code of LSTM and dataset can be downloaded from <https://web.njit.edu/~wangj/LSTMpredict/>.

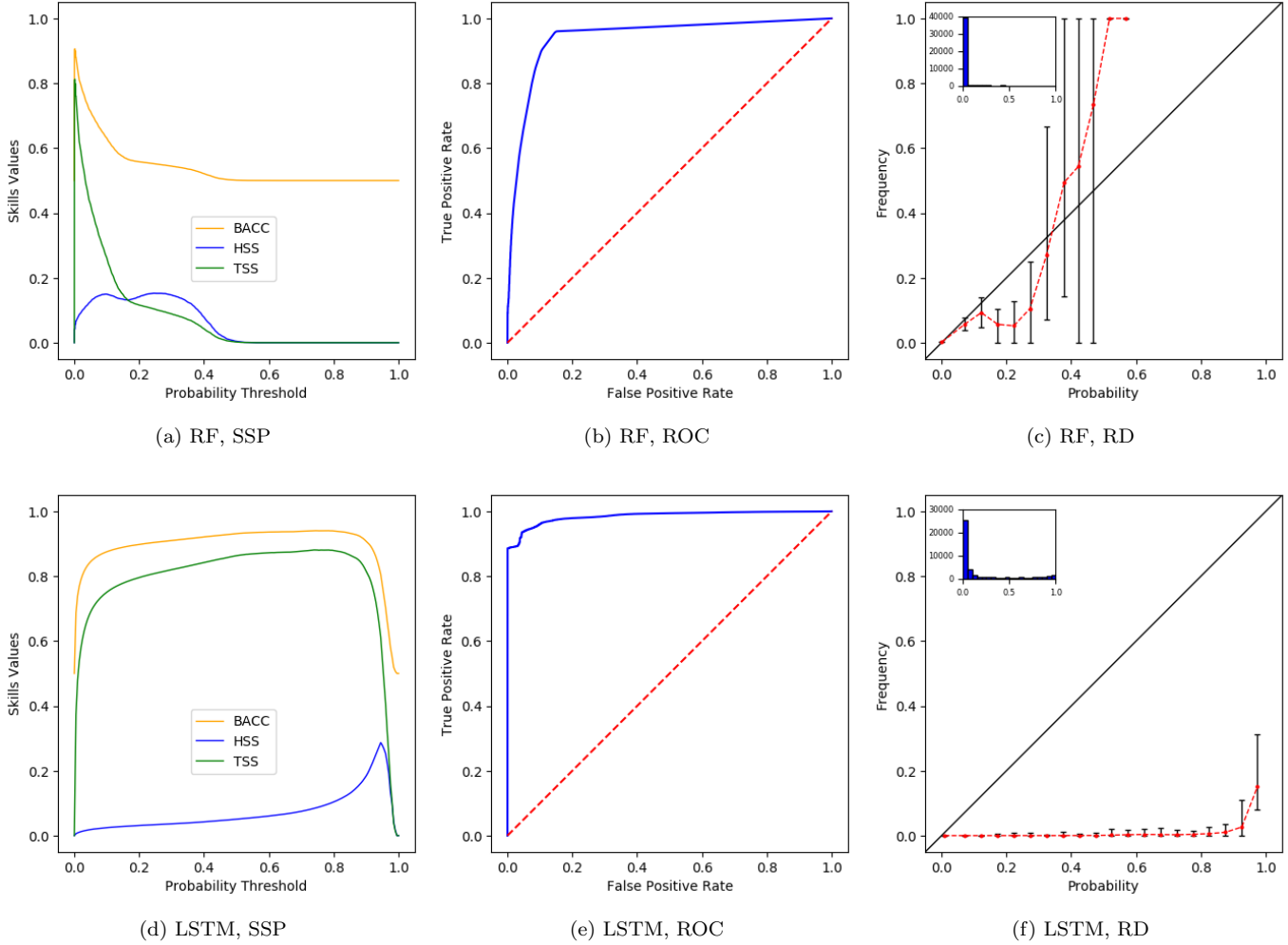


Figure 8. Comparison between RF (top) and LSTM (bottom) for $\geq M5.0$ -class flare prediction where the corresponding SSP, ROC and RD are displayed from left to right.

2010, 2011) to quantitatively assess the performance of probabilistic forecasting models. The values of BS range from 0 to 1 with the perfect score being 0. The values of BSS range from minus infinity to 1 with the perfect score being 1.

Figure 8 presents SSP, ROC and RD plots for RF and LSTM respectively when the methods are used in $\geq M5.0$ -class flare prediction. Refer to the SSP plots. For RF, the maximum TSS=0.812 is obtained with a probability threshold of 0.5%. With this threshold, BACC=0.906 \pm 0.014 and HSS=0.042 \pm 0.002. For LSTM, the maximum TSS=0.881 is obtained with a probability threshold of 75%. With this threshold, BACC=0.940 \pm 0.007 and HSS=0.084 \pm 0.015. The ROC curve of LSTM is better than that of RF. LSTM has an AUC of 0.984 \pm 0.003, which is better than RF with an AUC of 0.948 \pm 0.011. Refer to the RD plots. The curves of RF and LSTM are far away from the diagonal lines in the RD plots. The BS and BSS achieved by RF are 0.004 \pm 0.001 and 0.053 \pm 0.008 respectively. The BS and BSS achieved by LSTM are 0.090 \pm 0.011 and -21.576 \pm 2.956 respectively. In terms of BS and BSS, RF is better than LSTM.

Figure 9 presents SSP, ROC and RD plots for RF and LSTM respectively when the methods are used in $\geq M$ -class flare prediction. Refer to the SSP plots. For RF, the maximum TSS=0.768 is obtained with a probability threshold of 5%. With this threshold, BACC=0.884 \pm 0.003 and HSS=0.262 \pm 0.004. For LSTM, the maximum TSS=0.792 is obtained with a probability threshold of 60%. With this threshold, BACC=0.896 \pm 0.004 and HSS=0.323 \pm 0.030. The ROC curve of LSTM is slightly better than that of RF. LSTM has an AUC of 0.948 \pm 0.003, which is better than RF with an AUC of 0.935 \pm 0.002. Refer to the RD plots. The curve of RF is closer to the diagonal than the curve of LSTM. The BS and BSS achieved by RF are 0.021 \pm 0.001 and 0.260 \pm 0.006 respectively. The BS and BSS achieved

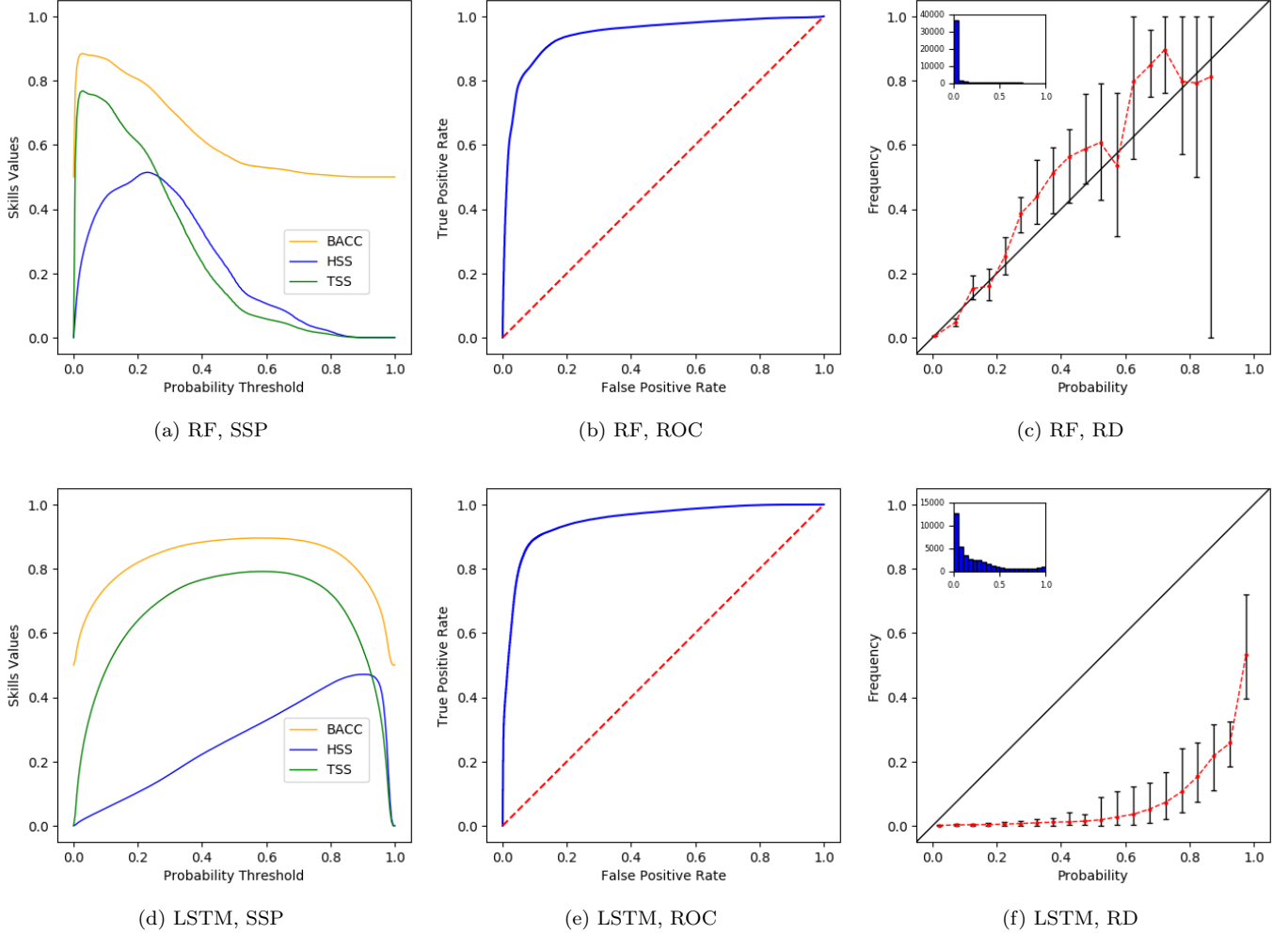


Figure 9. Comparison between RF (top) and LSTM (bottom) for $\geq M$ -class flare prediction where the corresponding SSP, ROC and RD are displayed from left to right.

by LSTM are 0.090 ± 0.009 and -2.241 ± 0.319 respectively. These results suggest that RF be a better probabilistic forecasting model than LSTM.

Figure 10 presents SSP, ROC and RD plots for RF and LSTM respectively when the methods are used in $\geq C$ -class flare prediction. Refer to the SSP plots. For RF, the maximum TSS=0.552 is obtained with a probability threshold of 25%. With this threshold, BACC= 0.776 ± 0.001 and HSS= 0.469 ± 0.003 . For LSTM, the maximum TSS=0.612 is obtained with a probability threshold of 50%. With this threshold, BACC= 0.806 ± 0.004 and HSS= 0.526 ± 0.021 . The ROC curve of LSTM is better than that of RF. LSTM has an AUC of 0.871 ± 0.002 , which is better than RF with an AUC of 0.851 ± 0.001 . Refer to the RD plots. The curve of RF almost overlaps the diagonal. The BS and BSS achieved by RF are 0.103 ± 0.001 and 0.344 ± 0.002 respectively. The BS and BSS achieved by LSTM are 0.133 ± 0.007 and 0.152 ± 0.047 respectively. These results indicate that RF is better than LSTM when the methods are used as probabilistic forecasting models.

5. DISCUSSION AND CONCLUSIONS

We develop a long short-term memory (LSTM) network to predict whether an AR would produce a Υ -class flare within the next 24 hours. We consider three Υ classes, namely $\geq M5.0$ class, $\geq M$ class, and $\geq C$ class, and build three LSTM models separately, each corresponding to a Υ class. Each LSTM model is used to make predictions of its corresponding Υ -class flares. We build a dataset containing the data in the period from 2010 May to 2018 May, gathered from the JSOC website. Each sample in the dataset has 40 features, including 25 magnetic parameters

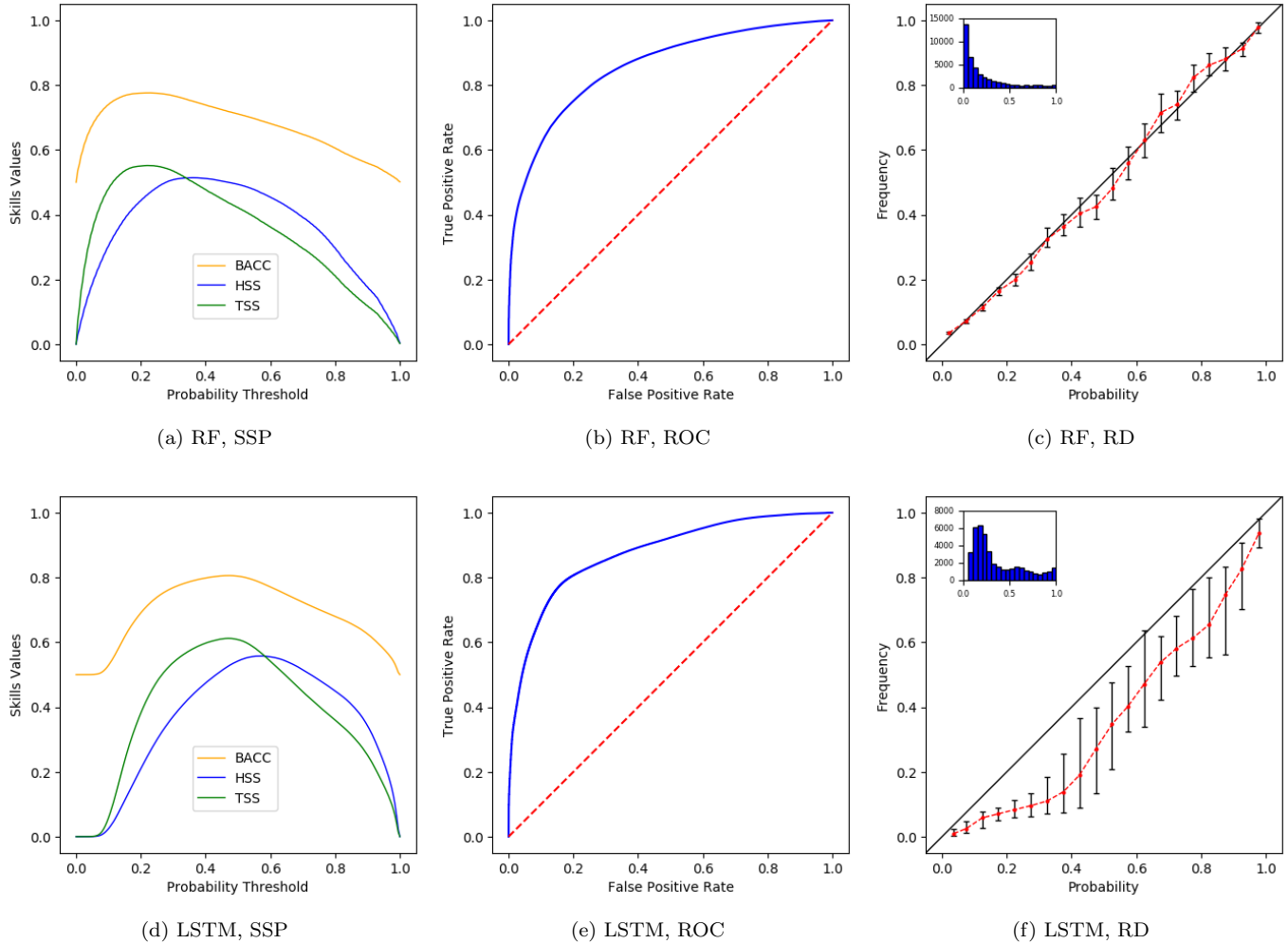


Figure 10. Comparison between RF (top) and LSTM (bottom) for $\geq C$ -class flare prediction where the corresponding SSP, ROC and RD are displayed from left to right.

provided by SHARP and related data products as well as 15 flare history parameters. We divide the dataset into three subsets: the subset covering 2010–2013 for training, the subset covering 2014 for validation, and the subset covering 2015–2018 for testing. The training subset and testing subset are disjoint, and hence our proposed method will make predictions on ARs that it has never seen before. With extensive experiments, we evaluate the performance of all three LSTM models and compare them with closely related machine learning methods using different performance metrics. The main results are summarized as follows.

1. Solar data samples in an AR are considered as time series in this study. Although some researchers (Nishizuka et al. 2017; Jonas et al. 2018) utilize information concerning flaring history for solar flare forecasts, none of the previous studies model the data samples as time series and adopt LSTMs to capture dependencies in the temporal domain of the data samples. To our knowledge, this is the first attempt of using LSTMs for solar flare prediction.
2. We evaluate the importance of each of the 40 features used in this study. Our experimental results show that, among these 40 features, 10 *SDO*/HMI magnetic parameters including TOTUSJH, TOTBSQ, TOTPOT, TOTUSJZ, ABSNJZH, SAVNCP, USFLUX, AREA_ACR, MEANPOT, TOTFX, and 6 flare history parameters including Cdec, Chis, Chis1d, Edec, Mhis and Xmax1d are more important than the other features for flare prediction. Our findings on the *SDO*/HMI magnetic parameters are mostly consistent with those reported in Bobra & Couvidat (2015). It was also observed that the history of C-class flares

contributes the most to flare prediction among all the flare history parameters. Although the rankings of the features are not the same for the three LSTM models, some features such as TOTUSJH, TOTUSJZ, TOTPOT, TOTBSQ, USFLUX, SAVNCP, Cdec, Chis and Chis1d exhibit great predictive power for all the three models. Furthermore, using only 14-22 most important features including both flare history and magnetic parameters can achieve better performance than using all the 40 features together.

3. Our LSTM-based approach achieves better performance than related machine learning methods such as multilayer perceptrons (MLP) (Haykin & Network 2004; Florios et al. 2018), Jordan network (JN) (Jordan 1997), support vector machines (SVM) (Qahwaji & Colak 2007; Yuan et al. 2010; Bobra & Couvidat 2015; Boucheron et al. 2015; Muranushi et al. 2015; Florios et al. 2018), and a recently published deep learning-based method, Deep Flare Net (DeFN; Nishizuka et al. 2018). In addition, we conduct an ablation study by considering three alternative architectures (ablations) LSTM_{-a}, LSTM_{-c} and LSTM_{-ac}. Our experimental results show that the proposed LSTM architecture achieves better performance than the three ablations, demonstrating the effectiveness of adding the attention layer and fully connected layers to LSTM units.

4. A related machine learning algorithm, namely random forests (RF) (Barnes et al. 2016; Liu et al. 2017; Florios et al. 2018), is comparable to our LSTM method. If one is interested in getting a probabilistic estimate of how likely an AR will produce a $\geq M5.0$ - ($\geq M$ -, $\geq C$ -, respectively) class flare within the next 24 hours, then RF would be the best choice. On the other hand, if one is interested in getting a firm answer regarding whether or not an AR will produce a $\geq M5.0$ - ($\geq M$ -, $\geq C$ -, respectively) class flare within the next 24 hours, then our LSTM method is significantly better than RF and is recommended.

Based on our experimental results, we conclude that the proposed LSTM-based framework is a valid method for solar flare prediction. Considering flare history parameters, besides *SDO*/HMI magnetic parameters, helps improve prediction performance, a finding consistent with that reported in Nishizuka et al. (2017) and Jonas et al. (2018). As solar data from various instruments are gathered at an unprecedented rate, some researchers attempt to employ additional features including solar images for flare prediction (Jonas et al. 2018). In future work, we plan to incorporate the image data into deep learning methods for predicting solar flares and other events (e.g., filament eruptions and CMEs).

We thank the referee for very helpful and thoughtful comments. We also thank the team of *SDO*/HMI for producing vector magnetic field data products. The X-ray flare catalogs were prepared by and made available through NOAA NCEI. The related machine learning methods studied in this work were implemented in Python. C.L. and H.W. acknowledge the support of NASA under grants NNX16AF72G, 80NSSC17K0016, 80NSSC18K0673 and 80NSSC18K1705.

REFERENCES

- Ahmed, O. W., Qahwaji, R., Colak, T., et al. 2013, *SoPh*, 283, 157, doi: [10.1007/s11207-011-9896-1](https://doi.org/10.1007/s11207-011-9896-1)
- Alpaydin, E. 2009, *Introduction to machine learning* (MIT press)
- Bahdanau, D., Cho, K., & Bengio, Y. 2014, *CoRR*, abs/1409.0473. <https://arxiv.org/abs/1409.0473>
- Barnes, G., Leka, K. D., Schrijver, C. J., et al. 2016, *ApJ*, 829, 89, doi: [10.3847/0004-637X/829/2/89](https://doi.org/10.3847/0004-637X/829/2/89)
- Benvenuto, F., Piana, M., Campi, C., & Massone, A. M. 2018, *ApJ*, 853, 90, doi: [10.3847/1538-4357/aaa23c](https://doi.org/10.3847/1538-4357/aaa23c)
- Bloomfield, D. S., Higgins, P. A., McAteer, R. T. J., & Gallagher, P. T. 2012, *ApJL*, 747, L41, doi: [10.1088/2041-8205/747/2/L41](https://doi.org/10.1088/2041-8205/747/2/L41)
- Bobra, M. G., & Couvidat, S. 2015, *ApJ*, 798, 135, doi: [10.1088/0004-637X/798/2/135](https://doi.org/10.1088/0004-637X/798/2/135)
- Bobra, M. G., Sun, X., Hoeksema, J. T., et al. 2014, *SoPh*, 289, 3549, doi: [10.1007/s11207-014-0529-3](https://doi.org/10.1007/s11207-014-0529-3)
- Boucheron, L. E., Al-Ghreibah, A., & McAteer, R. T. J. 2015, *ApJ*, 812, 51, doi: [10.1088/0004-637X/812/1/51](https://doi.org/10.1088/0004-637X/812/1/51)
- Breiman, L. 2001, *Machine learning*, 45, 5
- Brier, G. W. 1950, *Monthly Weather Review*, 78, 1
- Colak, T., & Qahwaji, R. 2009, *Space Weather*, 7, S06001, doi: [10.1029/2008SW000401](https://doi.org/10.1029/2008SW000401)
- Daglis, I., Baker, D., Kappenman, J., Panasyuk, M., & Daly, E. 2004, *Space Weather*, 2, S02004, doi: [10.1029/2003SW000044](https://doi.org/10.1029/2003SW000044)
- Fernández, S., Graves, A., & Schmidhuber, J. 2007, in *Proceedings of the 17th International Conference on Artificial Neural Networks, Part II*, 220–229. https://doi.org/10.1007/978-3-540-74695-9_23

- Fisher, G. H., Bercik, D. J., Welsch, B. T., & Hudson, H. S. 2012, *SoPh*, 277, 59, doi: [10.1007/s11207-011-9907-2](https://doi.org/10.1007/s11207-011-9907-2)
- Florios, K., Kontogiannis, I., Park, S.-H., et al. 2018, *SoPh*, 293, 28, doi: [10.1007/s11207-018-1250-4](https://doi.org/10.1007/s11207-018-1250-4)
- Goodfellow, I. J., Bengio, Y., & Courville, A. C. 2016, *Deep Learning, Adaptive computation and machine learning* (MIT Press). <http://www.deeplearningbook.org/>
- Graves, A., Fernández, S., Liwicki, M., Bunke, H., & Schmidhuber, J. 2007, in *Proceedings of the 21st Annual Conference on Neural Information Processing Systems*, 577–584
- Graves, A., Mohamed, A., & Hinton, G. E. 2013, in *Proceedings of the IEEE International Conference on Acoustics, Speech and Signal Processing*, 6645–6649. <https://doi.org/10.1109/ICASSP.2013.6638947>
- Graves, A., & Schmidhuber, J. 2005, *Neural Networks*, 18, 602, doi: [10.1016/j.neunet.2005.06.042](https://doi.org/10.1016/j.neunet.2005.06.042)
- Graves, A., & Schmidhuber, J. 2008, in *Proceedings of the 22nd Annual Conference on Neural Information Processing Systems*, 545–552
- Haykin, S., & Network, N. 2004, *Neural networks*, 2, 41
- He, H., & Garcia, E. A. 2009, *IEEE Trans. Knowl. Data Eng.*, 21, 1263, doi: [10.1109/TKDE.2008.239](https://doi.org/10.1109/TKDE.2008.239)
- Heidke, P. 1926, *Geografiska Annaler*, 8, 301
- Higgins, P. A., Gallagher, P. T., McAteer, R. T. J., & Bloomfield, D. S. 2011, *Advances in Space Research*, 47, 2105, doi: [10.1016/j.asr.2010.06.024](https://doi.org/10.1016/j.asr.2010.06.024)
- Hochreiter, S., & Schmidhuber, J. 1997, *Neural Computation*, 9, 1735, doi: [10.1162/neco.1997.9.8.1735](https://doi.org/10.1162/neco.1997.9.8.1735)
- Hopfield, J. J. 1982, *Proceedings of the National Academy of Sciences*, 79, 2554, doi: [10.1073/pnas.79.8.2554](https://doi.org/10.1073/pnas.79.8.2554)
- Huang, X., Zhang, L., Wang, H., & Li, L. 2013, *A&A*, 549, A127, doi: [10.1051/0004-6361/201219742](https://doi.org/10.1051/0004-6361/201219742)
- Jonas, E., Bobra, M., Shankar, V., Todd Hoeksema, J., & Recht, B. 2018, *SoPh*, 293, 48, doi: [10.1007/s11207-018-1258-9](https://doi.org/10.1007/s11207-018-1258-9)
- Jordan, M. I. 1997, in *Advances in psychology*, Vol. 121 (Elsevier), 471–495
- Kingma, D. P., & Ba, J. 2014, *CoRR*, abs/1412.6980. <https://arxiv.org/abs/1412.6980>
- Li, R., Cui, Y., He, H., & Wang, H. 2008, *Advances in Space Research*, 42, 1469, doi: [10.1016/j.asr.2007.12.015](https://doi.org/10.1016/j.asr.2007.12.015)
- Liu, C., Deng, N., Wang, J. T. L., & Wang, H. 2017, *ApJ*, 843, 104, doi: [10.3847/1538-4357/aa789b](https://doi.org/10.3847/1538-4357/aa789b)
- Luong, M., Pham, H., & Manning, C. D. 2015, *CoRR*, abs/1508.04025. <https://arxiv.org/abs/1508.04025>
- Marzban, C. 2004, *Weather and Forecasting*, 19, 1106
- Muranushi, T., Shibayama, T., Muranushi, Y. H., et al. 2015, *Space Weather*, 13, 778, doi: [10.1002/2015SW001257](https://doi.org/10.1002/2015SW001257)
- Nishizuka, N., Sugiura, K., Kubo, Y., Den, M., & Ishii, M. 2018, *ApJ*, 858, 113, doi: [10.3847/1538-4357/aab9a7](https://doi.org/10.3847/1538-4357/aab9a7)
- Nishizuka, N., Sugiura, K., Kubo, Y., et al. 2017, *ApJ*, 835, 156, doi: [10.3847/1538-4357/835/2/156](https://doi.org/10.3847/1538-4357/835/2/156)
- Park, S.-H., Lee, J., Choe, G. S., et al. 2008, *ApJ*, 686, 1397, doi: [10.1086/591117](https://doi.org/10.1086/591117)
- Pesnell, W. D., Thompson, B. J., & Chamberlin, P. C. 2012, *SoPh*, 275, 3, doi: [10.1007/s11207-011-9841-3](https://doi.org/10.1007/s11207-011-9841-3)
- Priest, E. R., & Forbes, T. G. 2002, *A&A Rv*, 10, 313, doi: [10.1007/s001590100013](https://doi.org/10.1007/s001590100013)
- Qahwaji, R., & Colak, T. 2007, *SoPh*, 241, 195, doi: [10.1007/s11207-006-0272-5](https://doi.org/10.1007/s11207-006-0272-5)
- Schmidhuber, J., Wierstra, D., & Gomez, F. J. 2005, in *Proceedings of the 19th International Joint Conference on Artificial Intelligence*, 853–858. <http://ijcai.org/Proceedings/05/Papers/1452.pdf>
- Schou, J., Scherrer, P. H., Bush, R. I., et al. 2012, *SoPh*, 275, 229, doi: [10.1007/s11207-011-9842-2](https://doi.org/10.1007/s11207-011-9842-2)
- Shibata, K., & Magara, T. 2011, *Living Reviews in Solar Physics*, 8, 6, doi: [10.12942/lrsp-2011-6](https://doi.org/10.12942/lrsp-2011-6)
- Song, H., Tan, C., Jing, J., et al. 2009, *SoPh*, 254, 101, doi: [10.1007/s11207-008-9288-3](https://doi.org/10.1007/s11207-008-9288-3)
- Steward, G., Lobzin, V., & Wilkinson, P. J. 2010, *AGU Fall Meeting Abstracts*, SH11B
- Sun, X., & for the CGEM Team 2014, arXiv:1405.7353
- SunPy Community, Mumford, S. J., Christe, S., et al. 2015, *Computational Science and Discovery*, 8, 014009, doi: [10.1088/1749-4699/8/1/014009](https://doi.org/10.1088/1749-4699/8/1/014009)
- Takasao, S., Fan, Y., Cheung, M. C. M., & Shibata, K. 2015, *ApJ*, 813, 112, doi: [10.1088/0004-637X/813/2/112](https://doi.org/10.1088/0004-637X/813/2/112)
- Wang, H. N., Cui, Y. M., Li, R., Zhang, L. Y., & Han, H. 2008, *Advances in Space Research*, 42, 1464, doi: [10.1016/j.asr.2007.06.070](https://doi.org/10.1016/j.asr.2007.06.070)
- Wilcoxon, F. 1947, *Biometrics*, 3, 119
- Wilks, D. S. 2010, *Quarterly Journal of the Royal Meteorological Society*, 136, 2109
- . 2011, *Statistical Methods in the Atmospheric Sciences*, Volume 100 (Academic Press)
- Winter, L. M., & Balasubramaniam, K. 2015, *Space Weather*, 13, 286, doi: [10.1002/2015SW001170](https://doi.org/10.1002/2015SW001170)
- Yu, D., Huang, X., Hu, Q., et al. 2010, *ApJ*, 709, 321, doi: [10.1088/0004-637X/709/1/321](https://doi.org/10.1088/0004-637X/709/1/321)
- Yu, D., Huang, X., Wang, H., & Cui, Y. 2009, *SoPh*, 255, 91, doi: [10.1007/s11207-009-9318-9](https://doi.org/10.1007/s11207-009-9318-9)
- Yuan, Y., Shih, F. Y., Jing, J., & Wang, H.-M. 2010, *Research in Astronomy and Astrophysics*, 10, 785, doi: [10.1088/1674-4527/10/8/008](https://doi.org/10.1088/1674-4527/10/8/008)